


Correlation between structural properties and iridescent colors of cellulose nanocrystalline films

M. Ličen · B. Majaron · J. Noh · C. Schütz ·
L. Bergström · J. Lagerwall · I. Drevenšek-Olenik 

Received: 1 July 2016 / Accepted: 1 September 2016 / Published online: 13 September 2016
© Springer Science+Business Media Dordrecht 2016

Abstract We investigate the effect of shear flow applied during the drying of aqueous suspension of cellulose nanocrystals on optical reflective properties and structural characteristics of the resulting solidified films. Shear flow can significantly improve internal structural homogeneity of the films, while its effect on optical reflective properties is relatively minor. The measured width of the selective reflection peak is an order of magnitude larger than expected for an ideal helically modulated structure, which reflects a distribution of pitch values and possibly also of regimes of distorted helical modulation. We attribute

these imperfections to the broad size distribution of the cellulose nanocrystals.

Keywords Cellulose nanocrystals · Chiral nematic liquid crystal · Iridescent films · Shear stress · Optical reflectance spectroscopy · Scanning electron microscopy

Introduction

Chirality is an inherent property of many natural molecules and systems, among them also cellulose fibres and crystallites (Conley et al. 2016). Due to the chirality of cellulose, concentrated aqueous suspensions of cellulose nanocrystals (CNC) exhibit the formation of a chiral nematic (cholesteric) liquid-crystalline phase (Revol et al. 1992). In this phase, rod-shaped CNC crystallites are orientationally aligned along a preferred local direction which twists in space in a left-handed helicoidal manner (Chandrasekhar 1992). When a droplet of such a suspension is deposited on a flat substrate and water is evaporated, a translucent solidified film with intriguing iridescent-colored appearance, similar to the glare of opals or nacre, is obtained (Revol et al. 1998). The iridescence is a consequence of selective optical reflection from the helical structure with periodicity in the range of wavelengths of visible light (John et al. 1995). This structure is a remnant of the cholesteric phase that is “locked-in” by vitrification during the drying process

M. Ličen · B. Majaron · I. Drevenšek-Olenik
Department of Complex Matter, J. Stefan Institute,
Jamova 39, 1000 Ljubljana, Slovenia

J. Noh · J. Lagerwall
Physics and Materials Science Research Unit, University
of Luxembourg, 162a, avenue de la Faiencerie,
L-1511 Luxembourg, Luxembourg

C. Schütz · L. Bergström
Department of Materials and Environmental Chemistry,
Stockholm University, Stockholm, Sweden

I. Drevenšek-Olenik (✉)
Faculty of Mathematics and Physics, University of
Ljubljana, Jadranska 19, 1000 Ljubljana, Slovenia
e-mail: irena.drevensek@ijs.si

C. Schütz
Department of Chemical Engineering, KU Leuven,
Campus Kulak Kortrijk, 8500 Kortrijk, Belgium

(Lagerwall et al. 2014; Wang et al. 2016). Despite many efforts to control formation and structure of drop-cast CNC films, a correlation between their structural details and optical reflective properties is still far from being satisfactorily resolved (Holt et al. 2010; Pan et al. 2010; Habibi et al. 2010; Beck et al. 2011, 2013; Salas et al. 2013; Dumanli et al. 2014a, b; Liu et al. 2014; Gray and Mu 2015; Wang and Walther 2015; Mu and Gray 2015).

Application of shear stress is an efficient method for manipulation of macro-scale orientation of the CNCs during the drying process (Orts et al. 1998; Ebeling et al. 1999; Cranston and Gray 2008; Hoeger et al. 2011; Diaz et al. 2013; Tatsumi et al. 2015). This method normally yields homogeneous films with CNCs aligned parallel to the shear flow direction. Consequently, it also inhibits formation of the helical modulation. However, our recent investigation revealed that a suitably weak circular shear flow generated during drying can lead to macroscopically uniform films that preserve helical modulation and display improved homogeneity of the iridescent colors (Park et al. 2014). This paper presents a comparative study of structural and optical properties of solution-cast CNC films prepared under the same drying conditions with or without the presence of a weak circular shear flow. Structural analysis by scanning electron microscopy (SEM) reveals that films exposed to shear flow exhibit superior homogeneity of their cross-sectional profile with respect to the films dried without shear flow. Rather surprisingly, however, optical reflective properties of both types of films are quite similar.

Experimental

Cellulose nanocrystals were prepared by sulfuric acid hydrolysis following (Gebauer et al. 2011). In detail, 20 g of dried “Domsjö wood” (sulfite softwood Domsjö Dissolving plus; Domsjö Fabriker AB, Domsjö, Sweden obtained from 60 % Norwegian spruce and 40 % Scots pine, with a hemicellulose content of 4.5 % and a lignin content of 0.6 %) was hydrolysed in 64 % H_2SO_4 (175 ml) for 60 min at 45 °C. The suspension was diluted 10 times with deionized (DI) water. The precipitate was repeatedly rinsed with DI water by centrifugation (20 min at 4754 g), and dialyzed against DI water for 5–7 days.

The suspension was sonicated for about 10 min at 70 % energy output using a Sonics Vibracell VC-750, USA) with a 13 mm wide titanium probe. The suspension was centrifuged in order to remove the introduced titanium particles and remaining aggregates and the resulting suspension was upconcentrated via slow evaporation. The colloidal stability results from sulfate half-ester groups, which provide a total charge of 0.3 mmol/g as determined by conductometric titration. These groups emanate from the sulfuric acid hydrolysis process. The CNCs have dimensions of 100–300 nm in length and 3–10 nm in width.

Two types of films were investigated in this study, both prepared from aqueous suspensions with concentration of 4.8 wt% and deposited on glass substrates with diameter of 25 mm. In one case, the film was left to dry on a still substrate. In the second, left-handed circular shear flow was induced during drying by placing the sample on an orbital mixer (Fine PCR SH30) with rotation speed of 44 rpm. This rotation speed was chosen because our previous investigation demonstrated good optical properties of the films obtained at this shear rate (Park et al. 2014). The drying process took place in a flow box at room temperature and lasted for about 12 h. A typical example of a dried film is shown in the inset of Fig. 1. A large central area of the film reflects blue-colored light. It is surrounded by several mm-wide rainbow-colored band, while the peripheral zone of the film has a dark red appearance, gradually turning into dark gray.

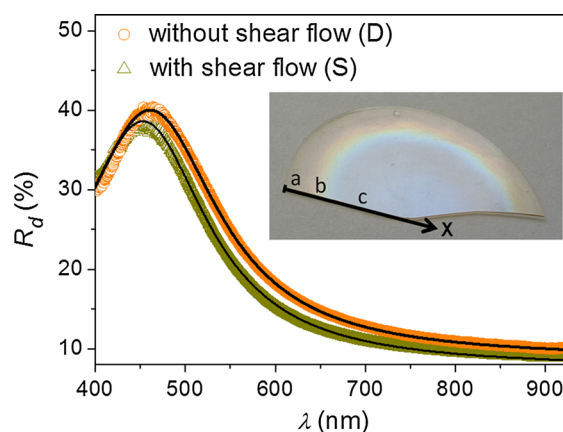


Fig. 1 Diffuse reflectance spectra measured at blue-colored central region of the two CNC films. *Black solid lines* are best fits of the Lorentzian line-shape. The *inset* shows a photo of the fractured sample S with the labels indicating areas with different optical properties

Diffuse reflectance spectra of both films were measured using an integrating sphere with an internal broad-band light source, fiber-coupled to a compact spectrometer sensitive in the 350–1050 nm spectral range (ISP-REF and USB4000, by Ocean Optics) (Vidovič and Majaron 2014). The samples were mounted onto a black-colored solid support and positioned at the integrating sphere's sample opening. Light reflected from the samples was collected at the signal port, positioned at an angle of 8° with respect to the sample normal. In order to obtain absolute reflectance values, the setup was calibrated using a commercial white standard with Lambertian reflectance $R_{wh} \geq 99\%$ (Spectralon[®], Labsphere). Reflectance spectra at different locations within each film were assessed by moving the samples laterally in steps of 0.50 or 0.25 mm using a linear translation stage. The effective diameter of the sensed surface area in each measurement was around 1.5 mm.

In addition, specular reflection of the films was measured using a linearly polarized collimated laser beam at 532 nm. The beam was incident on the film at an angle of 8° with respect to the sample normal. Light reflected from the film within the solid angle of $\sim 5 \times 10^{-3}$ sr along the direction of specular reflection was detected by a photodiode. The effective diameter of the laser beam on the sample was ~ 1 mm. Just like described above, the spatial dependence of the reflectivity was obtained by translating the sample in the lateral direction.

For SEM imaging of the cross-sectional structure, the samples were fractured by scribing a line on the glass substrate and then cracking the glass together with the films. After cracking, the film that was dried without shear flow has detached from the glass substrate and broke into several smaller pieces. The opposite effect was observed for the film prepared with shear flow: This film remained firmly attached to the glass substrate. Observed differences indicate that a detailed mechanical properties study is well motivated as a follow-up work of the investigations reported in this paper. Fractured pieces of the films were attached on a solid support using a carbon tape so that the fractured surface was oriented in the direction of imaging. The surface was coated with a thin Pt/Au layer. SEM images of the fractured surface were attained with a JEOL JSM-7600F electron microscope at operating voltage of 3 kV.

For Fourier analysis of the SEM images, the image was rotated so that the edge of the sample was parallel to the edge of the image. Fast Fourier transformation (FFT) of a selected region was performed line-by-line (in direction perpendicular to the structural layers) in *Mathematica* (Wolfram, v. 10.4) and the results were averaged over all lines. Before each transformation, the mean value of grayscale intensity of each line was subtracted from the data and a Hann window function was applied.

Results

Optical reflectance properties

In Fig. 1, we compare the diffuse reflectance spectra $R_d(\lambda)$ as measured in the central, blue-colored region of both samples (marked “c” in the inset). It is evident that the two spectra are very similar. Fitting of the reflectance peak with a Lorentzian line-shape yields a peak wavelength of $\lambda_{d,max} = 453 \pm 1$ nm and spectral width $\Delta\lambda_{FWHM} = 174 \pm 2$ nm for the film which was dried on still substrate (denoted in the following as film D). For the film that was dried in presence of shear flow (denoted in the following as film S), the results are $\lambda_{d,max} = 461 \pm 1$ nm and $\Delta\lambda_{FWHM} = 184 \pm 2$ nm, respectively.

Figure 2 shows diffuse reflectance spectra $R_d(\lambda)$ of the film D as measured at various distances x from its peripheral edge (for definition of x see the inset in Fig. 1). In the peripheral region (“a”; $x = 0\text{--}2.5$ mm), the reflectivity peaks appear at wavelengths between 600 and 700 nm, and the corresponding reflectance values $R_{d,max}$ increase with the distance from the sample edge (Fig. 2a). In the rainbow-colored region (“b”; $x = 2.5\text{--}7$ mm), in contrast, the reflectance peaks are shifting gradually from $\lambda_{d,max} = 650$ nm towards 450 nm, while the values of $R_{d,max}$ remain around 30 % (Fig. 2b). An increase of reflectance for $\lambda < 420$ nm that appears in all spectra is attributed to reflection from the non-perfect black tape that was used as an absorptive support for the samples. The spectra obtained for the film S were qualitatively similar and are therefore not presented.

The values of $\lambda_{d,max}$, $R_{d,max}$ and $\Delta\lambda_{FWHM}$ obtained from different locations in both types of CNC films are collected in Fig. 3. For film S, the values of $\lambda_{d,max}$ are decreasing with increasing x monotonically and more

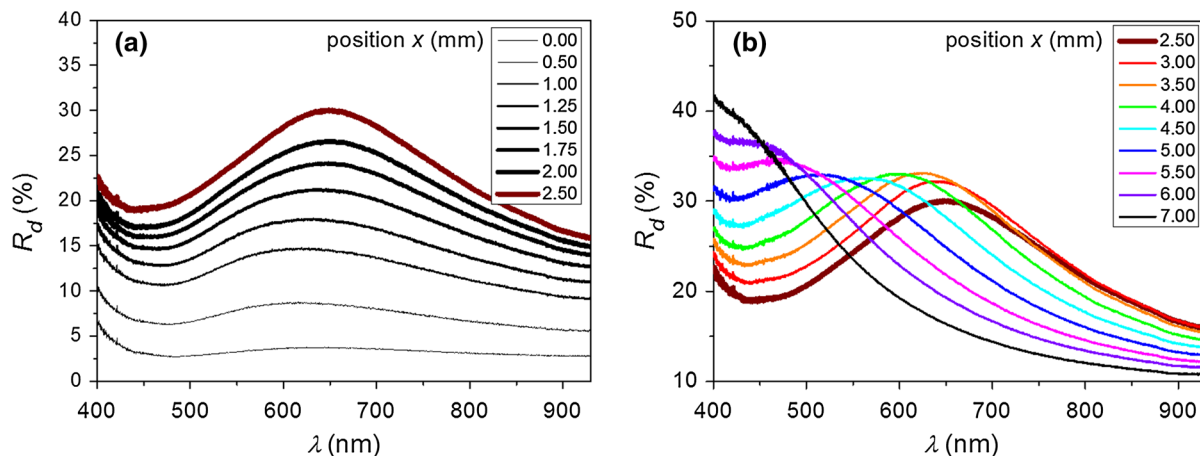


Fig. 2 Diffuse reflectance spectra of sample D measured at different positions from the outer edge of the CNC film: **a** dark red-colored peripheral region, $x = 0\text{--}2.5$ mm; **b** rainbow-colored transition region, $x = 2.5\text{--}7$ mm

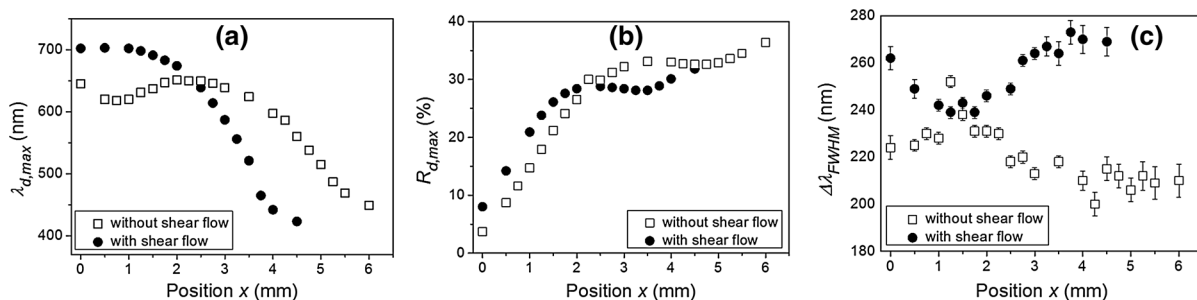


Fig. 3 Characteristic properties of diffuse reflectance spectra measured at different positions in CNC films dried with and without shear flow: **a** wavelength of the reflection peak, $\lambda_{d,max}$, **b** peak reflectance value, $R_{d,max}$, and **c** peak reflectance width ($\Delta\lambda_{FWHM}$)

rapidly as compared to film D (Fig. 3a). The dependencies of $R_{d,max}(x)$ of both films are quite similar: For small values of x , the values increase linearly with increasing x , but retain an approximately constant value after reaching $R_{d,max} \sim 30\%$ (Fig. 3b). The initial increase of $R_{d,max}$ is associated with increasing thickness of the CNC film in the peripheral region (Mu and Gray 2015). The dependencies of $\Delta\lambda_{FWHM}(x)$ for the two types of films differ more: At $x \sim 1.5$ mm, the film D exhibits a maximum, while the film S exhibits a minimum of $\Delta\lambda_{FWHM}$. The average values are $\langle\Delta\lambda_{FWHM}(x)\rangle = 218 \pm 12$ nm for sample D and $\langle\Delta\lambda_{FWHM}(x)\rangle = 261 \pm 12$ nm for sample S. This is approximately 50 nm more than the values observed in the central regions of the same samples.

The spatial dependence of the specular reflectance $R_s(x)$ as measured at 532 nm is shown in Fig. 4. This wavelength corresponds to selective reflection in a section within the rainbow-colored region of the films.

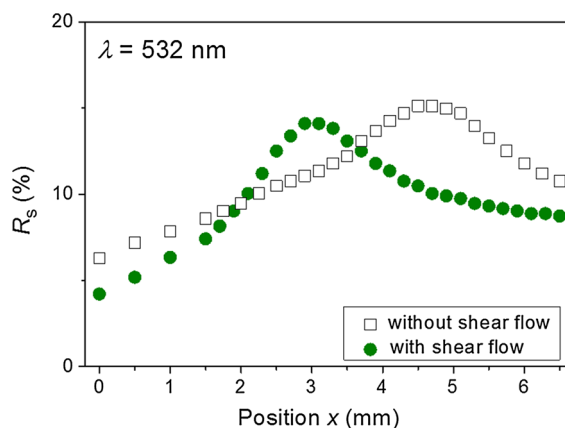


Fig. 4 Specular reflectance of the laser beam ($\lambda = 532$ nm) measured at different positions in both CNC film samples

In accordance with data shown in Fig. 3a, a maximum of R_s appears at a lower value of x for the film S (filled circles) than for the film D (empty squares). However,

the highest detected specular reflectance for both films is $R_{s,max} \sim 15\%$, which is around two times lower than observed in diffuse reflectance measurements (see Fig. 3b).

Structural properties

Figure 5 shows cross-sectional SEM images of two different lateral regions of the sample D. Parts of the film that were in contact with the glass substrate during the drying process (bottom-right area of the images) display a notable periodic structure, while the opposite parts, which were in contact with air (upper-left area of the images) show an irregular arrangement with no notable periodicity. Figure 5c shows a marked area in Fig. 5b imaged at larger magnification. A line corresponding to 10 structural periods (associated with

5-times helical periodicity p_h) is shown, which gives $p_h \sim 300$ nm.

The cross-sectional SEM images of the sample S reveal significantly different properties (Fig. 6). The entire cross-sectional areas exhibit a profound periodic assembly with the layers oriented parallel to the glass substrate. The periodicity is most evidently observable in Fig. 6b at the upper broken edge of the film, where bundles of CNC periodically protrude from the structure.

The variation of helical periodicity p_h with lateral distance x from the sample peripheral border is associated with presence of dislocations in the helical structure. An example of an area with several dislocations is shown in Fig. 7a. Besides this, the periodicity varies also with sample depth. This is illustrated in Fig. 7b, which shows the results of the FFT analysis

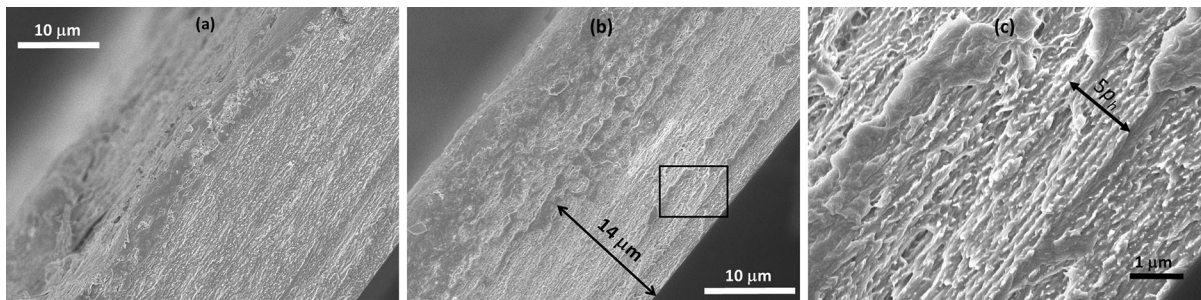


Fig. 5 Cross-sectional SEM images of the film that was dried without application of shear flow (film D) captured at different positions from the sample peripheral border: **a** red-colored edge region $x = 0\text{--}2.5$ mm, **b** blue-colored central region $x > 7$ mm. Upper-left regions of the images correspond to air–CNC film

interface and bottom-right regions to the CNC film–glass interface. **c** Marked area in (b) imaged at larger magnification. During the fracture process the film fully detached from the glass substrate and broke into smaller pieces

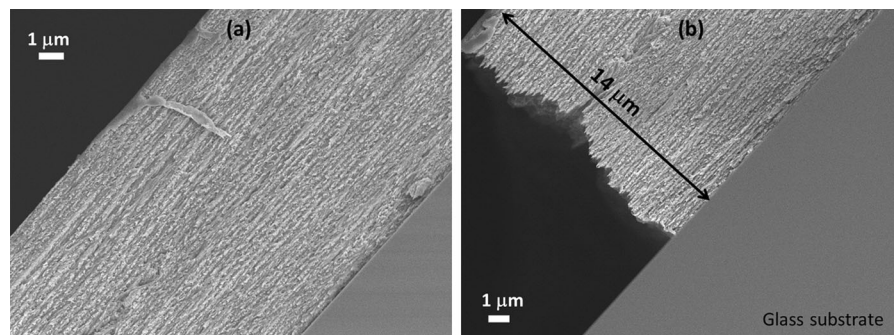


Fig. 6 Cross-sectional SEM images of the film that was dried with application of shear flow (film S) captured at different positions from the sample peripheral border: **a** red-colored edge region $x = 0\text{--}2.5$ mm, **b** rainbow-colored transition region

$x = 2.5\text{--}7$ mm. Upper-left regions of the images correspond to air–CNC film interface and down-right regions to the CNC film–glass interface. During the fracture process the film remained attached to the glass substrate

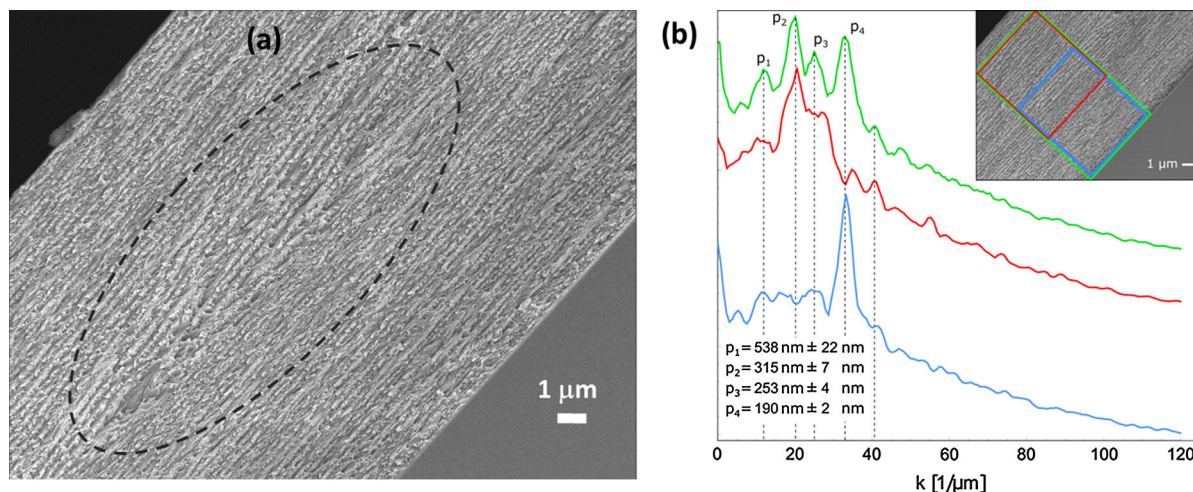


Fig. 7 **a** Cross-sectional SEM image of an area exhibiting several dislocations in the helical structure (film S, blue-colored region $x > 7$ mm). **b** 1D FFT spectra of different regions of the image demonstrating variations of the structural periodicity with

performed for three different areas of the SEM image given in the inset. The upper (green) FFT spectrum, corresponding to the largest analyzed area, displays four different structural periodicities denoted in the image as p_1 , p_2 , p_3 and p_4 . In contrast, the area corresponding to the smaller region near the glass substrate (blue curve) predominantly displays only the periodicity p_4 .

Discussion

The peak wavelength λ_0 of the photonic-band gap associated with the Bragg reflection from an infinitely thick helical structure with helical pitch p_h is given as (John et al. 1995):

$$\lambda_0 = \bar{n} \cdot p_h \cdot \cos\theta \quad (1)$$

and the spectral width of the peak $\Delta\lambda_{bg}$ is described by

$$\Delta\lambda_{bg} = \Delta n \cdot p_h, \quad (2)$$

where \bar{n} is the average refractive index, θ is the angle between the incident beam and the helical axis, and Δn is birefringence. Within the band-gap region, circularly polarized light matching the helical structure of the medium theoretically exhibits 100 % reflectivity, while reflectivity for the orthogonal circular polarization is close to zero (Belyakov 1992). Consequently, the reflectivity for unpolarized and for linearly

sample depth. The *inset* shows the corresponding SEM image together with three different analyzed regions (film S, rainbow-colored transition region $x = 2.5$ –7 mm)

polarized light, which were used in our investigations, is expected to be ≤ 50 %. The reported average refractive index and birefringence of the CNC films are $\bar{n} \sim 1.55$ and $\Delta n \sim 0.06$ (Dumanli et al. 2014a; Wang and Walther 2015; Cranston and Gray 2008; Frka-Petecic et al. 2015), respectively. These values give $\Delta\lambda_{bg} \sim 0.04\lambda_0/\cos\theta$, which for $\theta = 8^\circ$ and $410 \text{ nm} < \lambda_0 < 700 \text{ nm}$, as relevant for our diffuse reflectance measurements, results in $16 \text{ nm} < \Delta\lambda_{bg} < 28 \text{ nm}$. As evident from Fig. 3c, the values of $\Delta\lambda_{FWHM}$ observed in our experiments are by an order of magnitude larger.

A common reason for broadening of the Bragg reflection peak is finite thickness of the helical structure (Chandrasekhar 1992; John et al. 1995; Belyakov 1992). For $\Delta n \sim 0.06$, the spectral width of the peak is expected to be notably larger from the value given by Eq. (2), if the thickness of the film is in the range $d < 20p_h$ (John et al. 1995), which corresponds to $d < 5 \mu\text{m}$ for the blue-reflecting and to $d < 10 \mu\text{m}$ for the red-reflecting region, respectively. According to Figs. 5, 6 and 7, the thickness of periodic regions in our samples is evidently larger than these values, so finite thickness of the structure cannot explain the observed broadening of the reflectance peaks. Therefore, the broadening should originate from the structural imperfections.

The imperfections are associated with spatial variation of the helical pitch and with variations in

the orientation of helical axis with respect to the substrate. The latter affects the angle θ in Eq. (1) and the presence of these variations explains why specular reflectance measurements with laser light at 532 nm (Fig. 4) give lower values than diffuse reflectance measurements corresponding to the reflection peak at this wavelength (Fig. 3). This signifies that also variations of the orientation of helical axis have to be taken into account.

The main contribution to spectral broadening is attributed to variations of the helical pitch p_h . In the border regions of the samples (regions “a” and “b” in the inset of Fig. 1), lateral modifications most probably prevail, while in the central region (region “c” in the inset of Fig. 1) variations of p_h with sample depth are possibly predominant. By taking $\cos \theta = 1$ in Eq. (1) one can obtain a rough estimation for pitch variance:

$$(\Delta p_h/p_h) = (\Delta \lambda_0/\lambda_0) \sim (\Delta \lambda_{FWHM}/\lambda_{d,max}), \quad (3)$$

which, considering the data for the central blue-colored sample regions shown in Fig. 1, gives $\Delta p_h/p_h = 38 \pm 1 \%$ for the film D and $\Delta p_h/p_h = 40 \pm 1 \%$ for the film S, respectively. For the green-colored region ($\lambda_{d,max} = 550$ nm) the results shown in Fig. 3 give $\Delta p_h/p_h \sim 50 \%$ corresponding to $\Delta p_h \sim 180$ nm. This value obtained from the spectroscopic analysis is in very good agreement with the results of the FFT analysis of the SEM images shown in Fig. 7b, which give $\Delta p_h \sim (p_1 - p_2 + 2p_3 - 2p_4)/2 = 174.5 \pm 21$ nm. In this calculation we presumed that p_3 and p_4 represent the second harmonics of p_1 and p_2 , i.e. that they correspond to $p_h/2$ (Majoinen et al. 2012).

A spectral width $\Delta \lambda_{FWHM}$ in the range of 100–200 nm, as detected in the central region of our samples, was observed also in many other studies investigating dried CNC films prepared from various sources (Pan et al. 2010; Beck et al. 2011, 2013; Dumanli et al. 2014a; Liu et al. 2014). Therefore, it seems to be associated with an intrinsic irregularity of the helical periodicity of the CNC films. It very probably originates from distribution of lengths and diameters of the nano-crystallites. During the drying process crystallites of various sizes phase-separate into domains with different periodicities that contribute to different reflection colors (Dumanli et al. 2014a, b).

As a hypothesis for the different vertical structures, we propose that, in the case of a droplet at rest, kinetic

arrest of the top layer, where water evaporation is the fastest, takes place at an early stage during drying (Lagerwall et al. 2014; Bodiguel and Leng 2010), locking a largely disordered arrangement into place. In the final film this disordered regime ends up covering the much better ordered bottom section, which due to the slower evaporation of water inside could remain in the equilibrium cholesteric state long enough for the helix to align vertically, as influenced by the bottom substrate (Wang et al. 2016). In contrast, if the droplet is exposed to rotational shear stress, the constant mixing of the surface layer prevents localized increase in CNC concentration, cancelling out gradients and extending the time of equilibrium liquid crystalline state throughout the sample. In this way the helix can form vertically throughout the whole film.

The most intriguing puzzle of our study is the question, how films with evidently very different structural perfection can result in so similar optical reflective properties. The explanation is that reflection originates predominantly from the periodic regions of the films, and these are very similar for both types of the films. Films dried in the presence of shear flow exhibit only a periodic structure with thickness in the range 10–20 μm , while films dried without shear flow exhibit a periodic structure with about the same thickness (see Figs. 5b, 6b) that is covered with a top layer without periodic characteristics. This top layer is very probably in the unwound cholesteric phase (nematic). If the refractive index in this top layer varies smoothly on the scale of optical wavelengths, it does not cause much reflection or scattering, so it does not significantly contribute to the reflectance spectrum. On the other hand, due to its birefringence, the non-periodic layer can significantly modify the polarization state of optical radiation. Therefore it dominantly affects the appearance of samples in polarization optical microscopy (POM) (Park et al. 2014). Hence, one can conclude that POM resolves primarily the aperiodic parts of the solidified CNC structure, while reflectance and transmittance spectra resolve mainly the periodic regions.

Conclusions

Our results demonstrate that application of a weak circular shear flow during the drying process of solution cast CNC films can produce solidified films

with superior structural periodicity established through the entire film depth. We propose that this is due to the cancellation of concentration gradients due to the rotational shear flow, and the consequent delayed kinetic arrest at the surface layer, allowing a uniform equilibrium cholesteric arrangement with vertical helix to form throughout the sample. *In-situ* optical experiments performed during the drying process are needed to resolve further details of the film formation process. Nevertheless, the much improved surface adhesion and structural uniformity obtained by drying with rotational shear flow can be very interesting in attempts to utilize the self-organized helical CNC structures for realizing optical coatings with enhanced mechanical properties.

Acknowledgments ML, BM and IDO acknowledge financial support in the frame of the National Research Program of Slovenia P1-0192. LB and CS acknowledge the Wallenberg Wood Science Center (WWSC) for financial support. CS thanks the Research Foundation – Flanders (FWO) for funding under the Odysseus Grant (G.0C60.13N).

References

- Beck S, Bouchard J, Berry R (2011) Controlling the reflection wavelength of iridescent solid films of nanocrystalline cellulose. *Biomacromolecules* 12:167–172. doi:[10.1021/bm1010905](https://doi.org/10.1021/bm1010905)
- Beck S, Bouchard J, Chauve G, Berry R (2013) Controlled production of patterns in iridescent solid films of cellulose nanocrystals. *Cellulose* 20:1401–1411. doi:[10.1007/s10570-013-9888-4](https://doi.org/10.1007/s10570-013-9888-4)
- Belyakov VA (1992) Diffraction optics of complex-structured periodic media. Springer, New York
- Bodiguel H, Leng J (2010) Imaging the drying of colloidal suspension. *Soft Matter* 6:5451–5460. doi:[10.1039/C0SM00323A](https://doi.org/10.1039/C0SM00323A)
- Chandrasekhar S (1992) Liquid crystals, 2nd edn. Cambridge University Press, Cambridge
- Conley K, Godbout L, Whitehead MA, van de Ven TGM (2016) Origin of the twist of cellulosic materials. *Carbohydr Polym* 135:285–299. doi:[10.1016/j.carbpol.2015.08.029](https://doi.org/10.1016/j.carbpol.2015.08.029)
- Cranston ED, Gray DG (2008) Birefringence in spin-coated films containing cellulose nanocrystals. *Colloids Surf A* 325:44–51. doi:[10.1016/colsurfa.2008.04.042](https://doi.org/10.1016/colsurfa.2008.04.042)
- Diaz JA, Wu X, Martini A, Youngblood JP, Moon RJ (2013) Thermal expansion of self-organized and shear-oriented cellulose nanocrystal films. *Biomacromolecules* 14:2900–2908. doi:[10.1021/bm400794e](https://doi.org/10.1021/bm400794e)
- Dumanli AG, van der Kooij HM, Kamita G, Reisner E, Baumberg JJ, Steiner U, Vignolini S (2014a) Digital color in cellulose nanocrystal films. *ACS Appl Mater Interfaces* 6:12302–12306. doi:[10.1021/am501995e](https://doi.org/10.1021/am501995e)
- Dumanli AG, Kamita G, Landman J, van der Kooij H, Glover BJ, Baumberg JJ, Steiner U, Vignolini S (2014b) Controlled, bio-inspired self-assembly of cellulose-based chiral reflectors. *Adv Opt Mater* 2:646–650. doi:[10.1002/adom.201400112](https://doi.org/10.1002/adom.201400112)
- Ebeling T, Paillet M, Borsali R, Diat O, Dufresne A, Cavallé JY, Chanzy H (1999) Shear-induced orientational phenomena in suspensions of cellulose microcrystals, revealed by small angle X-ray scattering. *Langmuir* 15:6123–6126. doi:[10.1021/la990046+](https://doi.org/10.1021/la990046+)
- Frka-Petesic B, Sugiyama J, Kimura S, Chanzy H, Maret G (2015) Negative diamagnetic anisotropy and birefringence of cellulose nanocrystals. *Macromolecules* 48:8844–8857. doi:[10.1021/acs.macromol.5b02201](https://doi.org/10.1021/acs.macromol.5b02201)
- Gebauer D, Oliynyk V, Salajkova M, Sort J, Zhou Q, Bergström L, Salazar-Alvarez G (2011) A transparent hybrid of nanocrystalline cellulose and amorphous calcium carbonate nanoparticles. *Nanoscale* 3:3563–3566. doi:[10.1039/c1nr10681c](https://doi.org/10.1039/c1nr10681c)
- Gray DG, Mu X (2015) Chiral nematic structure of cellulose nanocrystal suspensions and films; polarized light and atomic force microscopy. *Materials* 8:7873–7888. doi:[10.3390/ma8115427](https://doi.org/10.3390/ma8115427)
- Habibi Y, Lucia LA, Rojas OJ (2010) Cellulose nanocrystals: chemistry, self-assembly, and applications. *Chem Rev* 110:3479–3500. doi:[10.1021/cr900339w](https://doi.org/10.1021/cr900339w)
- Hoeger I, Rojas OJ, Efimenko K, Velev OD, Kelley SS (2011) Ultrathin film coatings of aligned cellulose nanocrystals from a convective-shear assembly system and their surface mechanical properties. *Soft Matter* 7:1957–1967. doi:[10.1039/c0sm01113d](https://doi.org/10.1039/c0sm01113d)
- Holt BL, Stoyanov SD, Pelan E, Paunov VN (2010) Novel anisotropic materials from functionalised colloidal cellulose and cellulose derivatives. *J Mater Chem* 20:10058–10070. doi:[10.1039/c0jm0122g](https://doi.org/10.1039/c0jm0122g)
- John WDS, Fritz WJ, Lu ZJ, Yang DK (1995) Bragg reflection from cholesteric liquid crystals. *Phy Rev E* 51:1191–1198
- Lagerwall JPF, Schütz C, Salajkova M, Noh JH, Park JH, Scalia G, Bergström L (2014) Cellulose nanocrystal-based materials: from liquid crystal self-assembly and glass formation to multifunctional films. *NPG Asia Mater* 6:e80. doi:[10.1038/am.2013.69](https://doi.org/10.1038/am.2013.69)
- Liu D, Wang S, Ma Z, Tian D, Gu M, Lin F (2014) Structure-color mechanism of iridescent cellulose nanocrystal films. *RCS Adv* 4:39322–39331. doi:[10.1039/c4ra06268j](https://doi.org/10.1039/c4ra06268j)
- Majoinen J, Kontturi E, Ikkala O, Gray DG (2012) SEM imaging of chiral nematic films cast from cellulose nanocrystal suspensions. *Cellulose* 19:1599–1605. doi:[10.1007/s10570-012-9733-1](https://doi.org/10.1007/s10570-012-9733-1)
- Mu X, Gray DG (2015) Droplets of cellulose nanocrystal suspensions on drying give iridescent 3-D “coffee-stain” rings. *Cellulose* 22:1103–1107. doi:[10.1007/s10570-015-0569-3](https://doi.org/10.1007/s10570-015-0569-3)
- Orts WJ, Godbout L, Marchessault RH, Revol JF (1998) Enhanced ordering of liquid crystalline suspensions of cellulose microfibrils: a small angle neutron scattering study. *Macromolecules* 31:5717–5725
- Pan J, Hamad W, Straus SK (2010) Parameters affecting the chiral nematic phase of nanocrystalline cellulose films. *Macromolecules* 43:3851–3858. doi:[10.1021/ma902383k](https://doi.org/10.1021/ma902383k)
- Park JH, Noh JH, Schütz C, Salazar-Alvarez G, Scalia G, Bergström L, Lagerwall JFP (2014) Macroscopic control of helix orientation in films dried from cholesteric liquid-

- crystalline cellulose nanocrystal suspensions. *Chem-PhysChem* 15:1477–1484. doi:[10.1002/cphc.201400062](https://doi.org/10.1002/cphc.201400062)
- Revol JF, Bradford H, Giasson J, Marchessault RH, Gray DG (1992) Helicoidal self-ordering of cellulose microfibrils in aqueous suspension. *Int J Biol Macromol* 14:170–172
- Revol JF, Godbout L, Gray DG (1998) Solid self-assembled films of cellulose with chiral nematic order and optically variable properties. *J Pulp Pap Sci* 24:146–149
- Salas C, Nypelö T, Rodriguez-Abreu C, Carrillo C, Rojas OJ (2013) Nanocellulose properties and applications in colloids and interfaces. *Curr Opin Coll Interface Sci* 19:383–396. doi:[10.1016/j.cocis.2014.10.003](https://doi.org/10.1016/j.cocis.2014.10.003)
- Tatsumi M, Teramoto Y, Nishio Y (2015) Different orientation patterns of cellulose nanocrystal films prepared from aqueous suspensions by shearing under evaporation. *Cellulose* 22:2983–2992. doi:[10.1007/s10570-015-0722-z](https://doi.org/10.1007/s10570-015-0722-z)
- Vidovič L, Majaron B (2014) Elimination of single-beam substitution error in diffuse reflectance measurements using an integrating sphere. *J Biomed Opt* 19:027006. doi:[10.1117/1.JBO.19.2.027006](https://doi.org/10.1117/1.JBO.19.2.027006)
- Wang B, Walther A (2015) Self-assembled, iridescent, crustacean-mimetic nanocomposites with tailored periodicity and layered cuticular structure. *ACS Nano* 9:10637–10646. doi:[10.1021/acs.nano.5b05074](https://doi.org/10.1021/acs.nano.5b05074)
- Wang PX, Hamad WY, MacLachlan MJ (2016) Structure and transformation of tactoids in cellulose nanocrystal suspensions. *Nat Commun* 7:11515. doi:[10.1038/ncomms11515](https://doi.org/10.1038/ncomms11515)